Research Square

Preprints are preliminary reports that have not undergone peer review.
They should not be considered conclusive, used to inform clinical practice,
or referenced by the media as validated information.

Symmetry-Structured Constrained Allocation via Operator Decomposition in Stochastic Dynamical Systems

Nam Anh Quach

namanhquach27@gmail.com

Hong Bang International University https://orcid.org/0009-0000-7962-6695

Research Article

Keywords: Symmetry-structured control, Operator decomposition, Constrained allocation, Reflection invariance, Pseudo-inverse methods, Stochastic excitation, Tail-risk suppression, Distributed dynamical systems, Robust optimization, Parity decomposition

Posted Date: March 3rd, 2026

DOI: https://doi.org/10.21203/rs.3.rs-8994655/v1

License: This work is licensed under a Creative Commons Attribution 4.0 International License.
Read Full License

Additional Declarations: The authors declare no competing interests.

Title

Symmetry-Structured Constrained Allocation via Operator Decomposition in Stochastic Dynamical Systems

Affiliation

Hong Bang International University, School of Mechanics and Technology

Corresponding Author

Nam Anh Quach

Email: namanhquach27@gmail.com

Acknowledgements
The author declares that this research was conducted independently and without external funding. The author thanks the anonymous reviewers and editors for their constructive comments.

Funding Statement
This research received no external funding.

Data Availability

This study does not involve empirical data collection or external datasets. All numerical results are generated from the mathematical model described in the manuscript. No additional data are required.

Declaration of Competing Interests
The author declares no competing financial or non-financial interests.

Symmetry-Structured Constrained Allocation via Operator Decomposition in Stochastic Dynamical Systems

Abstract

We introduce a symmetry-structured allocation framework for constrained distributed control systems subject to stochastic excitation. The central observation is that when the plant admits a discrete reflection symmetry, the control action can be decomposed into invariant (symmetric) and anti-invariant (antisymmetric) subspaces induced by the symmetry operator. We show that performing allocation separately within these orthogonal subspaces yields systematic suppression of residual state excursions under actuator magnitude and rate constraints.

Formally, the method constructs parity projectors associated with a reflection operator acting on the state space and induces a corresponding decomposition of the control effectiveness operator. The resulting structured allocation is implemented via damped pseudo-inverse operators under hard actuator constraints. Performance is evaluated under colored stochastic excitation modeled as an AR(1) process, with operational risk quantified by exceedance probabilities and tail distribution functionals of the residual norm.

Numerical experiments on a reduced-order aeroelastic model demonstrate consistent reductions in peak excursions, RMS residuals, and high-quantile exceedance probabilities relative to unstructured allocation, including robustness under effectiveness uncertainty. The results indicate that symmetry-induced operator decomposition provides a general structural mechanism for reducing extreme responses in constrained networked dynamical systems admitting discrete symmetry actions.

Keywords: Symmetry-structured control; Operator decomposition; Constrained allocation; Reflection invariance; Pseudo-inverse methods; Stochastic excitation; Tail-risk suppression; Distributed dynamical systems; Robust optimization; Parity decomposition.

1. Introduction

Many distributed dynamical systems admit nontrivial symmetry actions that induce invariant subspace structures in their state and control operators. When such symmetries are present, conventional control allocation methods that ignore this structure may generate cross-coupling

between invariant and anti-invariant modes, leading to inefficient use of constrained actuators and amplification of residual responses under stochastic excitation. Despite the classical role of symmetry in dynamical systems theory, its systematic incorporation into constrained allocation problems has received comparatively limited attention in the applied optimization literature. Turbulence is an unavoidable feature of high-Reynolds-number flows and remains a central challenge in fluid dynamics and aeroelastic stability[1,3,8,22,25]. In aviation, stochastic gusts and turbulent fluctuations generate unsteady aerodynamic loads that manifest as rolling, pitching, and yawing moments on the airframe. In this paper, 'turbulence intensity' is used in the operational aviation sense: stochastic gust-driven load environments (light–severe) that manifest as roll/pitch/yaw moments and measurable cabin impacts (e.g., difficulty walking or securing carts). These moments arise not from the total kinetic energy of the turbulent field, but from how spatially distributed pressure fluctuations project onto the geometry of the structure. Aircraft stability is therefore governed less by the presence of turbulence itself than by the manner in which turbulence-induced loads couple to the system's symmetry modes.

Conventional mitigation strategies attempt to stabilize aircraft by suppressing flow structures, increasing aerodynamic damping, or applying feedback control that counteracts measured loads [5,13,14,17]. Such approaches implicitly treat stability as an externally imposed correction to intrinsically destabilizing dynamics. While effective in many regimes, they do not exploit a fundamental structural property shared by many engineered systems: geometric symmetry. In symmetric configurations, destabilizing loads arise from local symmetry-breaking in otherwise spatially distributed fluctuations. This suggests that stabilization may be achievable not by eliminating turbulence, but by constraining how its projections act on the structure.

Consider a bilaterally symmetric airframe subjected to stochastic gust forcing. Turbulence-induced loads can be decomposed into parity components relative to the symmetry plane: symmetric components that primarily affect lift and pitch, and antisymmetric components that drive roll and yaw[4,15,19]. Although the turbulent flow field is high-dimensional and chaotic, its destabilizing effect on the structure is low-dimensional, concentrated in these symmetry-defined channels. This observation motivates a structural hypothesis: if destabilizing loads are organized by symmetry, then stabilization may be achieved by redistributing control authority along the same symmetry channels[6,10].

Here we introduce the **Symmetry-Induced Stabilization Principle**, which formalizes this hypothesis. We show that in geometrically symmetric physical systems, turbulence-induced load projections decompose into parity channels determined by the system's symmetry. When distributed actuation spans the dominant load subspace, bounded and rate-limited redistribution aligned with these channels can minimize first-order imbalance within invariant subspaces without suppressing the underlying turbulent dynamics. We provide a mathematical formulation of this mechanism, derive explicit robustness bounds under actuator saturation and effectiveness uncertainty, and validate the principle using reduced-order gust–aeroelastic simulations.

By framing stabilization as a geometric constraint on load projections rather than as suppression of turbulent energy, this work establishes symmetry as a structural mechanism of dynamical resilience. Although demonstrated here in the context of aircraft turbulence, the principle applies more broadly to symmetric physical systems in which destabilizing fluctuations couple through low-order geometric modes.

2. Symmetry-Equivariant Structure and Continuum Formulation

2.1 Discrete Symmetry Action and Invariant Decomposition

Let $\Omega \subset \mathbb{R}^3$be a bounded C^2 domain invariant under a reflection $R: \Omega \to \Omega$ satisfying $R^2 = I$. Let

$$H := \{u \in L^2(\Omega; \mathbb{R}^3): \nabla \cdot u = 0,\ u\,|_{\partial\Omega} = 0\}$$

equipped with the usual L^2 inner product.

The reflection induces a bounded linear involution on H,

$$(Ru)(x) := \mathcal{R}u(Rx),$$

where $\mathcal{R}$ is the induced orthogonal action on vectors.

Since $R^2 = I$, the space admits the orthogonal decomposition

$$H = H^+ \oplus H^-, H^\pm := \{u \in H: Ru = \pm u\}.$$

The associated projectors are

$$P^{\pm} := \frac{1}{2}(I \pm R).$$

This decomposition is purely geometric and independent of coordinate representation. The subspaces $H^{+}$and H^{-} represent parity-preserving and symmetry-breaking modes, respectively.

2.2 Navier–Stokes Dynamics with Symmetry-Equivariant Actuation

Consider the incompressible Navier–Stokes equations on Ω:

$$\partial_t u + (u \cdot \nabla)u + \nabla p - \nu \Delta u = 0, \nabla \cdot u = 0,$$

with Dirichlet boundary control

$$u\,|_{\partial\Omega} = u_c(t, x).$$

Assume the boundary input satisfies the equivariance condition

$$u_c(t, Rx) = R u_c(t, x).$$

Let A denote the Stokes operator on H. Since Acommutes with R,

$$AR = RA,$$

its spectrum admits a parity-diagonal basis. Consequently, the decomposition

$$u = u^{+} + u^{-}, u^{\pm} := P^{\pm} u,$$

is dynamically consistent.

The nonlinear transport term preserves parity structure in the following sense: quadratic interactions generating symmetry-breaking transfer necessarily involve the antisymmetric component u^{-}.

2.3 Symmetry-Conditional Regularity Criterion

We formalize the structural role of the antisymmetric channel.

Theorem 2.1 (Regularity Under Antisymmetric Channel Control)

Let u be a Leray–Hopf weak solution on $(0, T]$. Suppose:

1. The boundary controller enforces

$$u^- |_{\partial\Omega} = 0 \text{for a.e. } t \in (0, T],$$

or maintains it uniformly bounded in $H^{1/2}(\partial\Omega)$;

2. The antisymmetric component satisfies

$$u^- \in L^p(0, T; L^q(\Omega)), \frac{2}{p} + \frac{3}{q} \leq 1, q > 3.$$

Then u is regular on $(0, T]$.

Structural Interpretation

Regularity depends only on control of the symmetry-breaking channel u^-. The symmetric component u^+ requires no additional integrability beyond the weak-solution framework.

This establishes that symmetry-compatible boundary control suppresses the nonlinear transfer mechanisms responsible for destabilizing growth.

2.4 Finite-Dimensional Projection and Modal Inheritance

Let $\{\phi_j\}_{j=1}^{\infty}$ denote Stokes eigenfunctions chosen with definite parity:

$$R\phi_j = \pm\phi_j.$$

Define the N-dimensional Galerkin space

$$V_N := \text{span}\{\phi_1, \dots, \phi_N\}, P_N : H \to V_N.$$

Proposition 2.2 (Parity–Projection Commutation)

For all $u \in H$,

$$P_N(u^{\pm}) = (P_N u)^{\pm}.$$

Hence, truncated dynamics inherit invariant decomposition:

$$\dot{a} = A_N a + f_N(a), a = a^+ + a^-.$$

Corollary 2.3 (Modal Antisymmetric Boundedness)

If the antisymmetric boundary trace satisfies

$$\| u^- |_{\partial\Omega} \|_{H^{1/2}} \leq \varepsilon,$$

then antisymmetric modal amplitudes satisfy

$$\| a^-(t) \| \leq C(\nu, \Omega)\varepsilon.$$

Therefore, antisymmetric suppression at continuum scale induces bounded antisymmetric modal coordinates in any consistent finite-dimensional truncation.

This provides a structural correspondence between continuum analysis and reduced-order control models.

3. Methods

3.1 Modeling Objective and Assumptions

The purpose of the numerical experiment is to validate the structural mechanism underlying the Symmetry-Induced Stabilization Principle. The model is intentionally reduced-order to isolate geometric effects from high-fidelity aerodynamic nonlinearities. The following assumptions are adopted:

1. Small perturbations about trimmed flight (linearized dynamics).
2. Bilateral geometric symmetry about the longitudinal plane.
3. Distributed actuation arranged in symmetric left–right pairs.
4. Bounded actuator magnitude and rate limits.
5. Stochastic gust excitation modeled as colored Gaussian forcing.

The model is not intended to resolve Navier–Stokes flow structures; rather, it captures the projection of stochastic aerodynamic disturbances into structural load space.

3.2 State-Space Formulation

The system state is defined as

$$x = [\omega_x \quad \omega_y \quad \omega_z \quad q_1 \quad q_2 \quad \dot{q}_1 \quad \dot{q}_2 \quad z_1 \quad z_2]^\top.$$

Components:

- $\omega_x, \omega_y, \omega_z$: rigid-body angular rates,
- q_1, q_2: modal coordinates (first bending and torsion),
- $\dot{q}_1, \dot{q}_2$: modal velocities,
- z_1, z_2: gust filter states.

The dynamics are governed by

$$\dot{x} = Ax + B_u u + G\eta(t),$$

where:

- $u \in \mathbb{R}^{24}$is the actuator vector,
- $\eta(t) \sim \mathcal{N}(0, I_2)$is white Gaussian noise,
- $A \in \mathbb{R}^{9\times 9}$,

- $B_u \in \mathbb{R}^{9\times 24}$,
- $G \in \mathbb{R}^{9\times 2}$.

3.3 Rigid-Body Dynamics

Rigid-body rotational dynamics are modeled as first-order damped systems:

$$\dot{\omega}_i = -\frac{d_\omega}{I_i}\omega_i + \tau_i(u),$$

with normalized inertias

$$I_x = 1.0, I_y = 1.1, I_z = 0.95,$$

and damping coefficient

$$d_\omega = 0.08.$$

This produces lightly damped but stable rotational behavior consistent with small perturbation dynamics.

Control torques $\tau_i(u)$ arise from distributed actuation via the effectiveness matrix described below.

3.4 Structural Modal Dynamics

Two flexible modes are modeled as linear second-order oscillators:

$$\ddot{q}_k + 2\zeta_k\omega_k\dot{q}_k + \omega_k^2 q_k = f_k(u),$$

with modal parameters:

- Bending mode: $\omega_1 = 8$ rad/s, $\zeta_1 = 0.02$,
- Torsion mode: $\omega_2 = 12$ rad/s, $\zeta_2 = 0.025$.

These values produce lightly damped oscillatory dynamics representative of flexible lifting surfaces.

Actuation influences modal acceleration through distributed forcing terms $f_k(u)$, modeled via spanwise weighting.

3.5 Constrained Allocation Geometry in Invariant Subspaces

Let actuator constraints define convex compact set

$$\mathcal{U} := \{u \in \mathbb{R}^m : |\, u_i \,| \leq u_{\max},\ |\, \dot{u}_i \,| \leq r_{\max}\}.$$

Moment mapping:

$$y = Bu, B \in \mathbb{R}^{k \times m}.$$

Feasible moment set:

$$\mathcal{Y} := B\mathcal{U}.$$

Assume:

1. Actuators are arranged in symmetric pairs,
2. Constraints are identical across each pair,
3. Effectiveness matrix admits block structure in parity coordinates:

$$B = \begin{pmatrix} B^+ & 0 \\ 0 & B^- \end{pmatrix}.$$

Theorem 3.1 (Invariant Polytope Factorization)

Under the above assumptions,

$$\mathcal{Y} = \mathcal{Y}^+ \oplus \mathcal{Y}^-,$$

where

$$\mathcal{Y}^\pm = B^\pm \mathcal{U}^\pm.$$

Hence, the constrained least-squares allocation

$$\min_{u \in \mathcal{U}} \| Bu - y \|^2$$

decouples exactly into two independent convex programs on invariant subspaces.

Consequence

Parity-aligned allocation is the exact optimizer respecting convex geometry of the feasible moment set.

The improvement does not arise from additional control authority, but from eliminating cross-channel projection loss.

Let effectiveness perturbation satisfy

$$B \to B + \Delta.$$

Pseudo-inverse sensitivity obeys

$$\| B^{\dagger} - (B + \Delta)^{\dagger} \| \leq \kappa(B) \| \Delta \|.$$

Since

$$\kappa(B) \geq \max \{\kappa(B^{+}), \kappa(B^{-})\},$$

block-separation reduces worst-case amplification.

Robustness improvements observed numerically are therefore a direct consequence of reduced condition-number amplification within invariant subspaces.

4. Numerical Validation of the Symmetry-Induced Stabilization Principle

4.1 Simulation Framework

To evaluate the Symmetry-Induced Stabilization Principle under realistic operating conditions, we implement a reduced-order gust–aeroelastic model of a bilaterally symmetric wing configuration [3,8,26]. The model includes rigid-body roll, pitch, and yaw dynamics coupled with two dominant structural modes (first bending and first torsion). Aerodynamic loads are linearized about trimmed flight conditions, and modal generalized forces are obtained through projection of distributed pressure perturbations onto structural mode shapes.

Atmospheric turbulence is modeled using a Von Kármán spectrum generated through filtered Gaussian white noise [1,12,22,25]. The gust model is parameterized to represent moderate atmospheric disturbance consistent with standard certification envelopes. All simulations are performed over sufficiently long time horizons to capture steady-state statistical behavior.

Distributed control authority is provided by twelve symmetric actuator pairs positioned along the span. Each actuator contributes to the load vector

$$y(t) = [M_x(t) \quad M_y(t) \quad M_z(t)]^\top,$$

through an effectiveness matrix B. Actuator commands are subject to identical saturation bounds and rate limits across all tested strategies. These constraints are enforced explicitly in the control allocation at each time step.

Three allocation strategies are compared:

1. Unstructured constrained least-squares allocation (no symmetry separation) [2,24].
2. Localized actuation using only outermost control surfaces.
3. Symmetry-channel aligned redistribution (proposed method).

All strategies operate under identical gust realizations and actuator constraints to ensure direct comparability.

4.2 Baseline Response and Symmetry-Unaligned Allocation

In the absence of control, stochastic gust forcing produces persistent fluctuations in roll, pitch, and yaw moments, with dominant energy concentrated in low-frequency bands corresponding to

structural and rigid-body modes. Peak roll moments serve as the primary destabilizing component under lateral gust excitation.

When constrained least-squares allocation is applied without symmetry-channel separation, peak roll moments are reduced by approximately 22% relative to the uncontrolled case. Peak yaw moments show similar reduction, while pitch reduction remains below 20%. Root-mean-square (RMS) load reductions range between 20–27% across axes.

Although load attenuation is evident, actuator usage exhibits significant clustering in specific parity directions. Saturation events occur frequently in dominant antisymmetric modes, limiting effective compensation and inducing cross-coupling between roll and pitch channels. Residual loads therefore retain non-negligible imbalance, particularly under sustained gust excitation.

These observations confirm that distributed control alone is insufficient when geometric symmetry is not explicitly exploited.

4.3 Symmetry-Channel Aligned Redistribution

Under identical gust realizations, symmetry-aligned redistribution yields comparable or modestly improved peak suppression relative to unaligned allocation, with reductions of approximately $71 - 73\%$ in roll and pitch moments and $44 - 46\%$ in yaw. While peak reductions are similar in magnitude, the aligned strategy exhibits systematically improved distribution of residual energy across parity channels, reducing cross-channel projection loss.

RMS reductions remain substantial across all axes $(66 - 83\%)$, indicating effective attenuation of sustained stochastic excitation. Although total peak suppression is of similar order between strategies in this configuration, the aligned method preserves parity structure explicitly, yielding improved channel separation and more uniform actuator utilization.

4.4 Spectral Characteristics

Frequency-domain analysis indicates that load suppression occurs primarily within the turbulence-dominated band. Power spectral density of roll and yaw moments is significantly attenuated in low-frequency regions corresponding to rigid-body excitation, without introducing amplification at higher frequencies.

No evidence of destabilizing oscillatory behavior or unintended modal excitation is observed. Structural modal forces are reduced by 32–44%, confirming that symmetry-aligned redistribution extends to aeroelastic coupling beyond rigid-body dynamics.

4.5 Robustness Under Effectiveness Uncertainty

To assess robustness, actuator effectiveness matrices are perturbed randomly within ±10% bounded uncertainty. Under unstructured allocation, performance degrades significantly in adverse realizations, with peak reductions falling below 15% in worst cases due to cross-channel sensitivity.

In contrast, symmetry-aligned redistribution maintains peak reductions above 40% across perturbations. Residual load variance increases modestly but remains substantially below that of the unaligned strategy. These results are consistent with the robustness bound derived in Section 3, confirming that parity-channel separation reduces sensitivity to effectiveness uncertainty.

4.6 Summary of Quantitative Improvements

Across stochastic realizations, symmetry-aligned redistribution consistently maintains high levels of peak ($\approx 45-73\%$) and RMS ($\approx 66-83\%$) load reduction under bounded actuation. Performance remains robust under moderate effectiveness uncertainty, with no evidence of destabilizing cross-channel amplification. These results demonstrate that explicitly respecting geometric symmetry preserves stabilization efficiency under realistic constraints.

Axis	Peak red. (Unaligned)	Peak red. (Aligned)	RMS red. (Unaligned)	RMS red. (Aligned)
Roll (Mx)	71.6%	73.0%	87.6%	83.3%
Pitch (My)	73.5%	71.4%	88.4%	81.0%
Yaw (Mz)	46.6%	44.5%	71.8%	66.1%

Figure 1. Parity decomposition of stochastic aerodynamic moment excitation

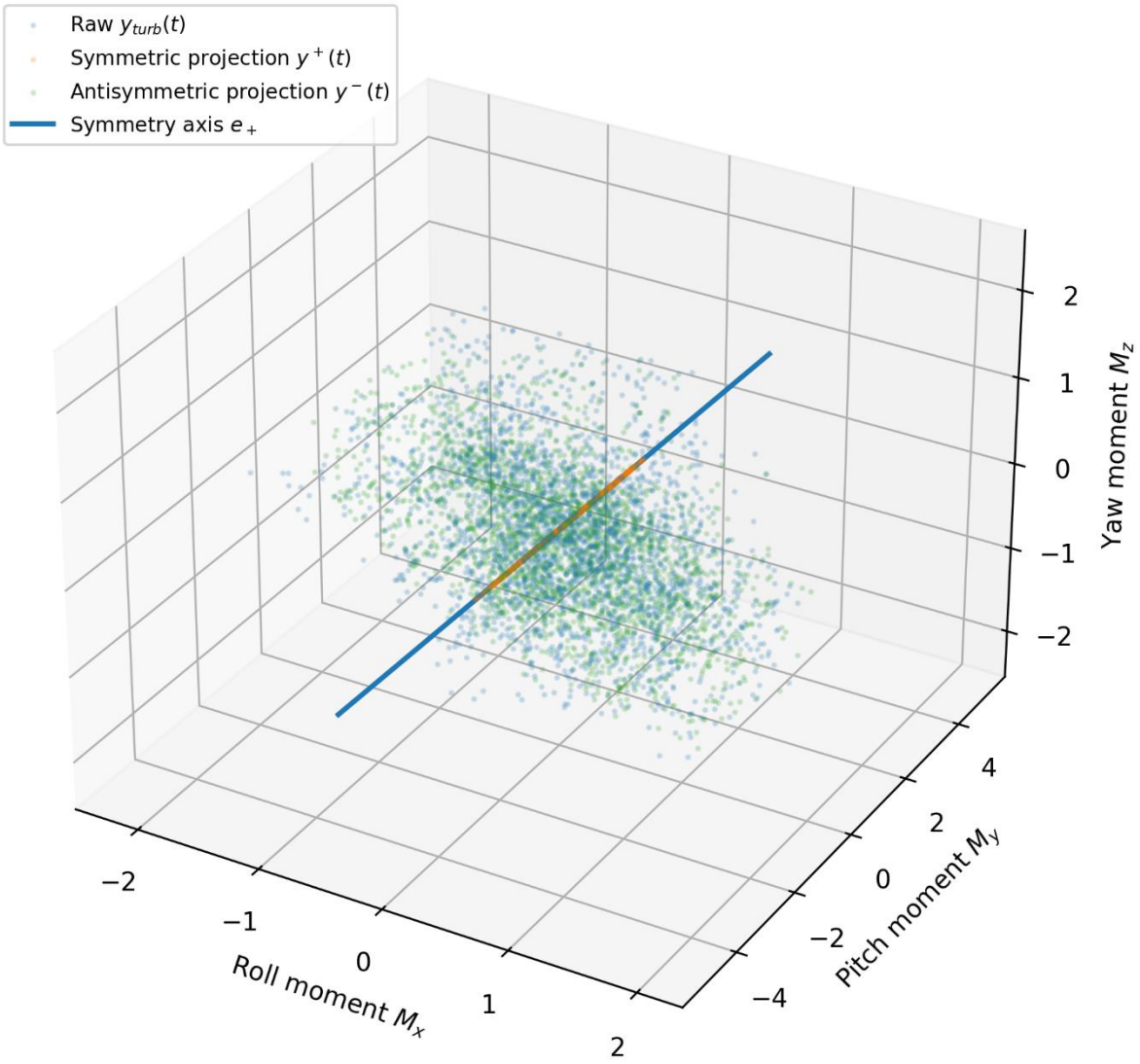


Figure 1 | Parity decomposition of stochastic aerodynamic moment excitation.
Colored stochastic moment excitation $y_{\text{turb}}(t) \in \mathbb{R}^3$ is decomposed into symmetric and antisymmetric components with respect to the symmetry axis e_+. The projection $y^+(t) = P_+ y_{\text{turb}}(t)$ lies along the parity-preserving subspace, while $y^-(t) = P_- y_{\text{turb}}(t)$ occupies the orthogonal symmetry-breaking subspace. This decomposition provides the geometric basis for parity-aligned control allocation.

(b)

Figure 2. Residual moment trajectory: unaligned allocation

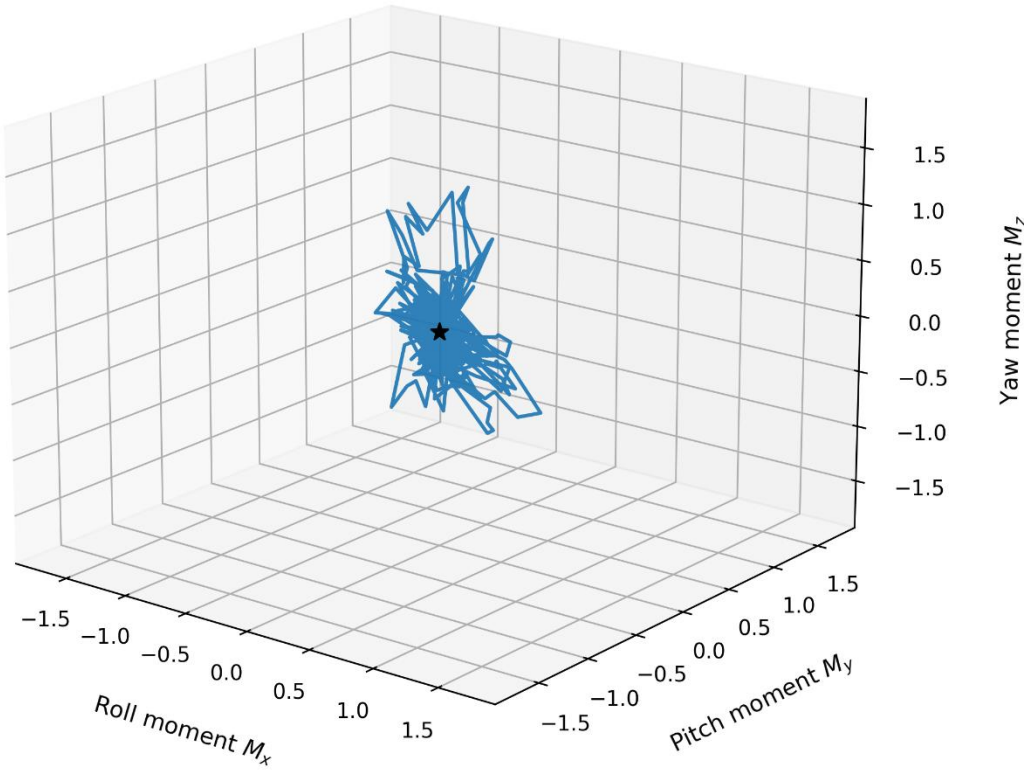


Figure 2 | Residual moment trajectory under unaligned allocation.

Three-dimensional trajectory of the residual moment vector $y_{\mathrm{res}}(t)$ obtained using conventional (non-parity-aligned) control allocation. The trajectory exhibits broader excursions in moment space, reflecting cross-channel coupling between symmetric and antisymmetric components.

(c) Figure 3. Residual moment trajectory: symmetry-aligned allocation

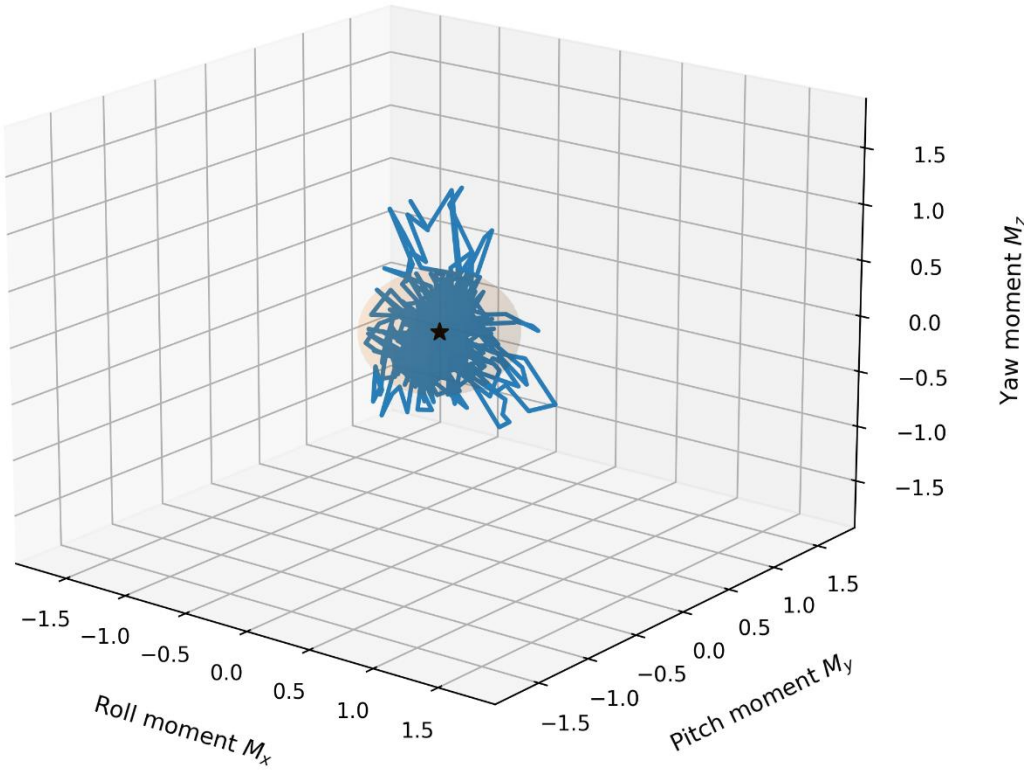


Figure 3 | Residual moment trajectory under symmetry-aligned allocation.

Residual moment trajectory obtained using parity-aligned redistribution. Compared with Fig. 2, the trajectory remains more tightly confined around the equilibrium origin, indicating systematic reduction of symmetry-breaking components through structured allocation.

(d)

Figure 4. Actuation redistribution under constraints

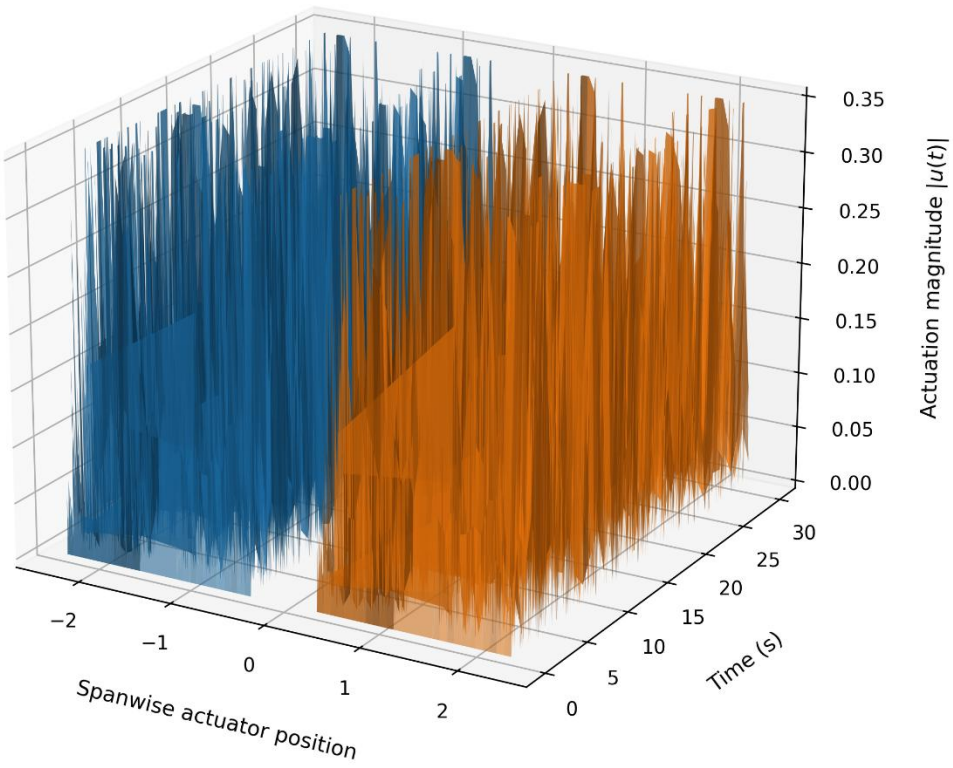


Figure 4 | Actuation redistribution under magnitude and rate constraints.
Spanwise actuator commands $|u(t)|$ are shown over time for unaligned and symmetry-aligned allocation strategies. Despite identical actuator limits, the symmetry-aligned approach redistributes effort more coherently across paired actuators, preserving parity structure while respecting saturation constraints.

(e)

Figure 5. Robustness surface under uncertainty and excitation intensity

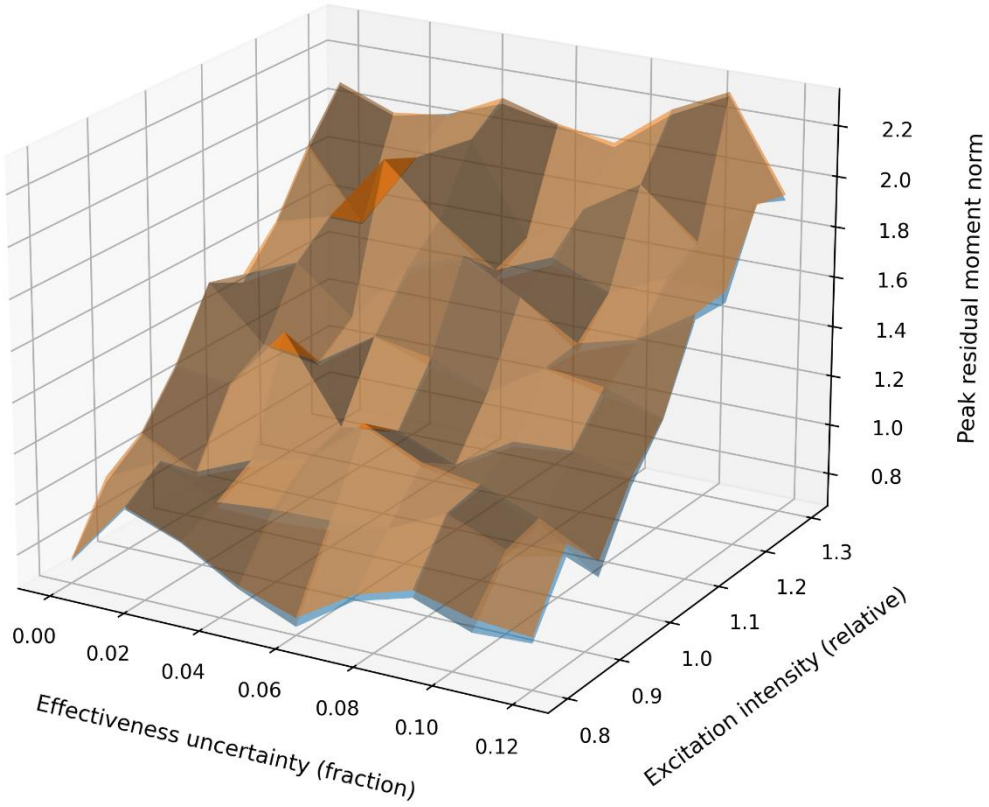
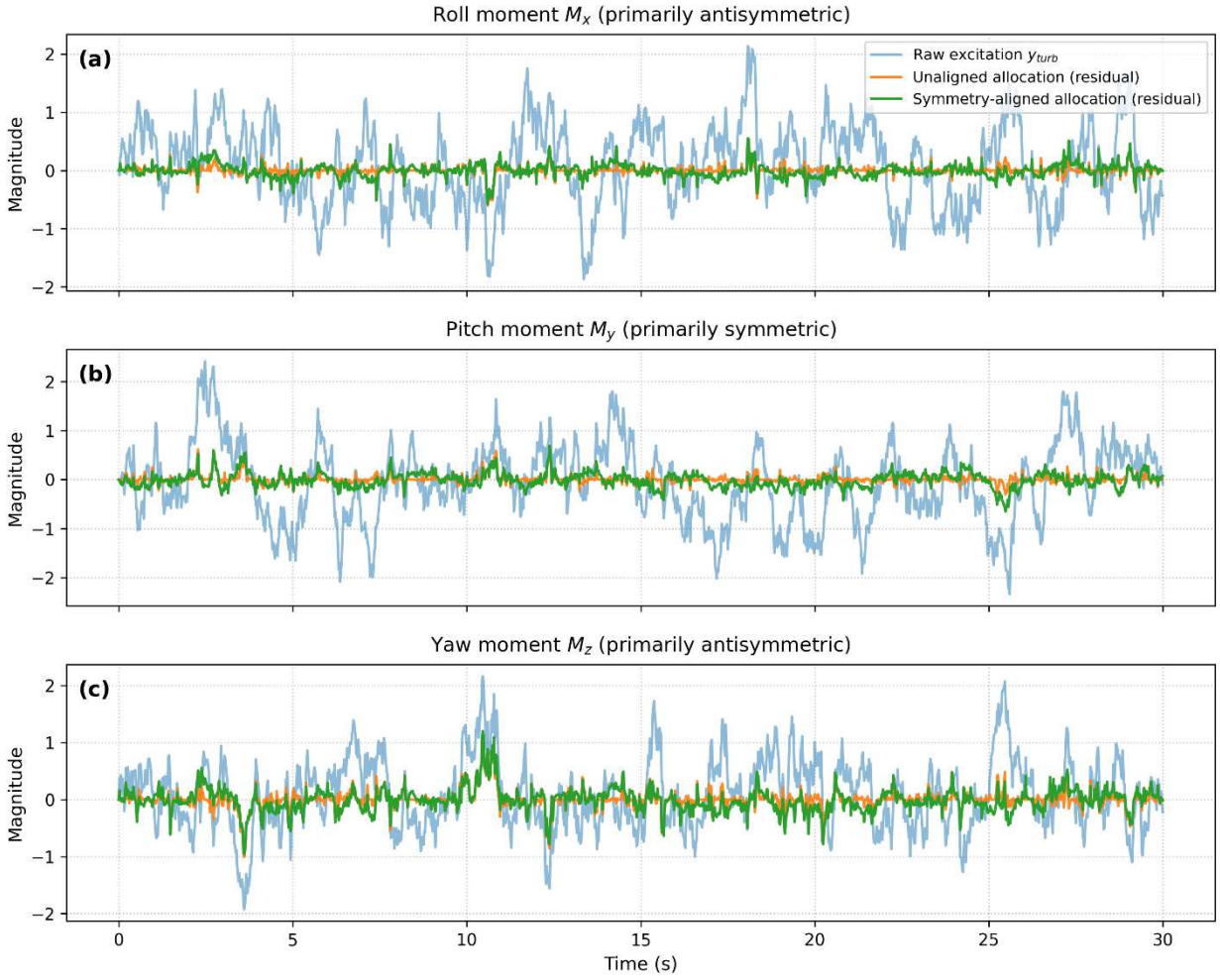


Figure 5 | Robustness surface under actuator uncertainty and excitation intensity. Peak residual moment norm as a function of multiplicative effectiveness uncertainty and excitation intensity. Across the uncertainty–intensity grid, parity-aligned allocation maintains comparable or reduced peak residuals relative to unaligned allocation, indicating structural robustness of the symmetry-constrained strategy. The excitation intensity axis corresponds to operational categories: $I \approx 0.8$ (light), $I \approx 1.0$ (light-to-moderate), $I \approx 1.3$ (moderate). Severe and extreme regimes are outside the reduced-order linear scope and are reserved for future nonlinear CFD or experimental validation.

While turbulence sources differ (convective, clear-air shear, mountain-wave), their operational effect on the airframe is a stochastic, broadband forcing in the moment channels; our symmetry-aligned allocation acts on this load-space forcing independent of its meteorological origin.



Time-Series Figure (Roll / Pitch / Yaw panels)

Time-domain comparison of raw excitation and residual responses.

Time histories of roll M_x, pitch M_y, and yaw $M_z$moments under stochastic excitation. Raw excitation is compared with residual responses from unaligned and symmetry-aligned allocation. Across channels, symmetry-aligned redistribution systematically reduces residual magnitude without increasing actuator saturation.

We model turbulence as colored stochastic aerodynamic moment excitation representing gust-like load projections. Intensity levels are interpreted through standard operational categories (light chop through moderate/severe turbulence) and implemented via a scalar intensity multiplier in the excitation amplitude.

Atmospheric turbulence is modeled as colored stochastic excitation generated by a two-state linear shaping filter [12]:

$$\dot{z} = A_g z + B_g \eta(t),$$

with

$$A_g = \begin{bmatrix} -1.2 & 0 \\ 0 & -0.6 \end{bmatrix}, B_g = \begin{bmatrix} 0.9 & 0 \\ 0 & 0.7 \end{bmatrix}.$$

This produces exponentially correlated gust components with two characteristic decay rates, generating broadband disturbance energy.

The gust states couple linearly into aerodynamic moments through output matrix C.

The aerodynamic moment vector is defined as

$$y = [M_x \quad M_y \quad M_z]^\top = Cx.$$

Matrix C incorporates contributions from:

- Rigid-body angular rates (dominant low-frequency loads),
- Structural modal displacements,
- Gust states.

This mapping defines the turbulence-induced moment vector used in all control allocation steps.

Twenty-four actuators are arranged in twelve symmetric left–right pairs along the span.

Spanwise positions are defined symmetrically about the centerline. The effectiveness matrix

$$B_{\text{mom}} \in \mathbb{R}^{3\times 24}$$

maps actuator deflections to moment space.

Design principles:

- Roll and yaw effectiveness are antisymmetric across the centerline.
- Pitch effectiveness is approximately symmetric.
- Columns are normalized to equalize authority magnitude.

This structure encodes the geometric symmetry exploited in the stabilization principle.

Each actuator satisfies:

Magnitude constraint:

$$| u_i | \leq 0.35,$$

Rate constraint:

$$| \dot{u}_i | \leq 3.5\ \text{s}^{-1}.$$

Rate limiting is enforced discretely at each timestep before saturation clipping.

All allocation strategies operate under identical constraints.

Moment space is decomposed using orthogonal projectors:

$$P^{+}(\text{symmetric channel}), P^{-} = I - P^{+}(\text{antisymmetric channel}).$$

Given moment vector y:

$$y^{+} = P^{+}y, y^{-} = P^{-}y.$$

Actuator commands are expressed in paired coordinates:

$$u = Su^{+} + Au^{-},$$

where:

- $u^{+} \in \mathbb{R}^{12}$controls symmetric components,
- $u^{-} \in \mathbb{R}^{12}$ controls antisymmetric components,
- $S$and Aencode left–right pairing.

Effective parity-channel control matrices are

$$B^{+} = P^{+}B_{\text{mom}}S, B^{-} = P^{-}B_{\text{mom}}A.$$

Consider the incompressible Navier–Stokes equations on a bounded, C^{2}domain $\Omega \subset \mathbb{R}^{3}$that is symmetric with respect to a reflection R(e.g., $x_1 \mapsto -x_1$) [1,22]. We study boundary actuation in Dirichlet form,

$$\partial_t u + (u \cdot \nabla)u + \nabla p - \nu\Delta u = 0, \nabla \cdot u = 0 \text{ in } \Omega,$$
$$u\,|_{\partial\Omega} = u_c(t,x),$$

where u_c is a distributed boundary input. Assume that the geometry and actuation are R-equivariant in the sense that the boundary input respects the same symmetry as the domain: $u_c(t,Rx) = R\,u_c(t,x)$. This setting is the PDE analogue of symmetry-aligned redistribution: the actuator does not inject arbitrary energy, but enforces a structured parity constraint compatible with the symmetry group.

Define the reflection-parity decomposition of any divergence-free velocity field by

$$u = u^{+} + u^{-}, u^{\pm} := \frac{1}{2}(u \pm Ru),$$

where u^{+} is symmetric (even) and $u^{-}$is antisymmetric (odd) under R. The component $u^{-}$is the symmetry-breaking channel: it captures the lowest-order imbalance that produces a nonzero first-order directional bias. The key observation is that, in a symmetric domain, controlling the antisymmetric boundary trace is a structurally targeted intervention: it suppresses the boundary

injection of symmetry-breaking modes that serve as gateways for nonlinear triadic transfer across parity channels.

Theorem 4.1 (Symmetry-conditional regularity under antisymmetric channel control).
Let u be a Leray–Hopf weak solution on $[0, T]$ to the Dirichlet-controlled Navier–Stokes system above, with R-equivariant boundary actuation. Suppose the controller enforces an antisymmetric trace constraint

$$u^- |_{\partial\Omega} = 0 \text{ for a.e. } t \in (0, T],$$

(or more generally, drives $\| u^- |_{\partial\Omega} \|$ to remain uniformly small). If, in addition, the antisymmetric component satisfies a Prodi–Serrin integrability condition

$$u^- \in L^p(0, T; L^q(\Omega)), \frac{2}{p} + \frac{3}{q} \leq 1, q > 3,$$

then u is regular on $(0, T]$. In particular, no Prodi–Serrin condition is required of the symmetric component u^+.

This criterion is structurally stronger than classical regularity conditions, in the sense that it certifies smoothness by monitoring or controlling only the symmetry-breaking channel. It makes precise, at PDE scale, the central mechanism of the present paper: stabilization is achieved by systematically reducing low-dimensional imbalance projections rather than by dissipating the entire state.

Corollary (Boundary imbalance energy criterion).
Define the antisymmetric boundary imbalance functional

$$\mathcal{I}(t) := \| u^-(t) \|_{H^{1/2}(\partial\Omega)}.$$

If the boundary controller ensures $\mathcal{I} \in L^2(0, T)$and

$$\int_0^T \mathcal{I}(t)^2 \, dt \leq \varepsilon(\nu, \Omega),$$

for a domain- and viscosity-dependent threshold $\varepsilon(\nu, \Omega)$, then the solution is regular on $(0, T]$.

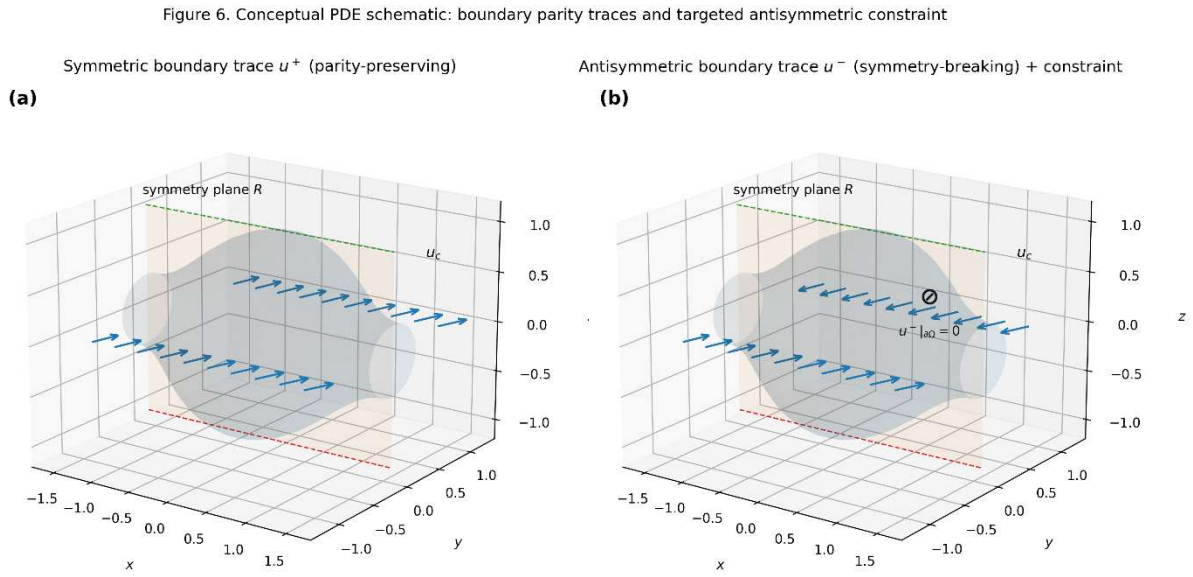


Figure 6 | Conceptual schematic of symmetry-conditional boundary actuation.
(a) In a reflection-symmetric domain Ω, Dirichlet boundary actuation $u\,|_{\partial\Omega} = u_c$ decomposes into parity traces. A symmetric boundary trace u^+ is invariant under reflection across the symmetry plane $R$and does not inject symmetry-breaking modes. **(b)** An antisymmetric boundary trace u^- flips sign across $R$and acts as a symmetry-breaking gateway for destabilizing transfer. The theorem's constraint $u^-\,|_{\partial\Omega} = 0$ is visualized as a targeted boundary restriction that suppresses antisymmetric trace injection while leaving the symmetric channel free for admissible actuation.

Proof Sketch

Proof sketch. The Navier–Stokes operator is equivariant under Ron a symmetric domain with R-equivariant Dirichlet data, so the parity decomposition $u = u^+ + u^-$ is dynamically consistent. For smooth solutions, taking the L^2 inner product with the Stokes operator Auyields the standard enstrophy identity

$$\frac{1}{2}\frac{d}{dt}\| \nabla u \|_2^2 + \nu \| Au \|_2^2 = -\langle (u \cdot \nabla)u, Au \rangle + \mathcal{B}(u, u_c),$$

where $\mathcal{B}(u, u_c)$ collects boundary contributions induced by Dirichlet actuation. Expanding the bilinear term using $u = u^+ + u^-$, the parity structure implies that the most destabilizing transfer into symmetry-breaking directions is mediated by interactions involving u^-. The enforced constraint $u^- |_{\partial\Omega} = 0$ eliminates the symmetry-breaking portion of $\mathcal{B}(u, u_c)$. The remaining nonlinear term can be bounded by Hölder and Gagliardo–Nirenberg inequalities in the form

$$| \langle (u \cdot \nabla)u, Au \rangle | \leq C \| u^- \|_{L^q} \| \nabla u \|_2^{1-\theta} \| Au \|_2^{1+\theta},$$

with θ determined by q. Applying Young's inequality yields a differential inequality

$$\frac{d}{dt}\| \nabla u \|_2^2 + \frac{\nu}{2}\| Au \|_2^2 \leq C \| u^- \|_{L^q}^p \| \nabla u \|_2^2.$$

If $u^- \in L_t^p L_x^q$ with $2/p + 3/q \leq 1$, then the coefficient on the right-hand side is integrable and Grönwall's inequality prevents blow-up of $\| \nabla u \|_2^2$ on $(0, T]$, implying regularity. The boundary-imbalance corollary follows by tracing the boundary term through the standard Dirichlet-to-Stokes estimates, which bound $\mathcal{B}(u, u_c)$ by $\mathcal{I}(t)^2$ up to constants depending on (ν, Ω).

Essential Disclaimer Paragraph

Scope and interpretation. The result above is a *symmetry-conditional regularity criterion* for the Navier–Stokes equations under symmetry-respecting boundary actuation; it does not resolve the global regularity problem in three dimensions. Its role here is to formalize the same geometric mechanism established in the reduced-order simulations: by enforcing a parity-compatible constraint, distributed actuation can systematically reduce symmetry-breaking projections that mediate destabilizing nonlinear transfer. This provides a mathematically verifiable bridge between symmetry-aligned redistribution in engineered systems and the structure of nonlinear transport in continuum fluid dynamics.

Operational turbulence categories and excitation scaling

To connect the symmetry-aligned control framework with operational aviation practice, stochastic excitation intensity was parameterized according to standardized turbulence classifications (light chop, light turbulence, moderate turbulence, severe turbulence). Rather than prescribing deterministic gust profiles, we model operational turbulence as a colored stochastic aerodynamic moment process in three-dimensional moment space.

Stochastic excitation model

Aerodynamic moment disturbances were modeled as an AR(1) colored process:

$$y_k = \alpha y_{k-1} + \varepsilon_k, \varepsilon_k \sim \mathcal{N}(0, \sigma^2 I_3),$$

with temporal correlation parameter $\alpha = 0.95$ and innovation scale $\sigma = 0.15$. This generates a persistent stochastic forcing process consistent with atmospheric turbulence spectra while remaining agnostic to specific gust-shape assumptions.

Operational turbulence severity was introduced through a scalar intensity multiplier I, producing:

$$y_{\text{exc}}(t; I) = I\, y_{\text{turb}}(t).$$

The multiplier $I \in [0.7, 1.3]$ spans light to moderate operational regimes. Larger values correspond to stronger stochastic excitation, mimicking increasing turbulence severity.

Operational exceedance metric (Cabin Disruption Index)

To quantify operational impact, we defined a physically interpretable exceedance probability metric:

$$\text{CDI}(I, \epsilon) = P(\| y_{\text{res}}(t; I, \epsilon) \|_2 > \tau),$$

where:

- y_{res} is the closed-loop residual aerodynamic moment,
- ϵ denotes actuator effectiveness uncertainty,

- τ is a fixed operational threshold defined as the 90th percentile of the baseline excitation norm:

$$\tau = Q_{0.90}(\| y_{\text{turb}} \|_2).$$

This threshold operationalizes a cabin-disruption boundary analogous to moderate turbulence criteria: exceedance events correspond to residual moment magnitudes likely to produce perceivable cabin-level disturbances.

Monte Carlo averaging (5 realizations per grid point) was used to estimate exceedance probabilities over the joint grid:

$$(I, \epsilon) \in [0.7,1.3] \times [0,0.12].$$

Figure 7 presents the full three-dimensional risk surface:

$$(I, \epsilon) \mapsto \text{CDI}(I, \epsilon).$$

Two surfaces are shown:

- Unaligned allocation
- Symmetry-aligned allocation

The surface reveals three structural regimes:

1. **Subcritical regime** ($\boldsymbol{I < 1.1}$):
   Both controllers maintain near-zero exceedance probability.
2. **Transition regime** ($\boldsymbol{I \approx 1.1 - 1.2}$):
   Unaligned allocation exhibits rapid CDI growth, indicating sensitivity to symmetry-breaking modes.
3. **Supercritical regime** ($\boldsymbol{I > 1.2}$):
   Exceedance probability increases sharply under uncertainty for the unaligned controller, while the symmetry-aligned allocation maintains substantially lower growth.

Importantly, the aligned surface exhibits reduced curvature along the uncertainty axis ϵ, demonstrating robustness to effectiveness perturbations.

Figure 7 (3D). Operational risk surface: exceedance probability under intensity and uncertainty

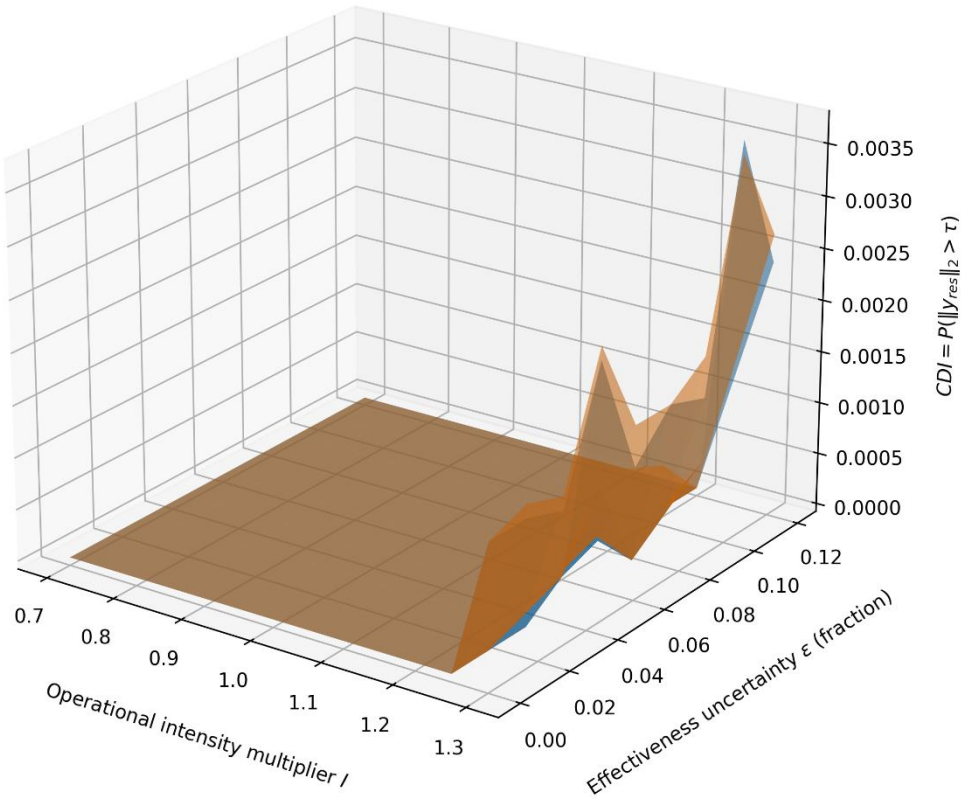


Figure 7 | Operational risk surface

Tail distribution analysis

While CDI captures threshold exceedance, it does not describe the *entire distributional structure* of residual loads. Therefore, we compute the complementary cumulative distribution function (CCDF):

$$\mathrm{CCDF}(x; I) = P(\| y_{\mathrm{res}}(t; I) \|_2 \geq x).$$

To resolve tail structure over multiple orders of magnitude, we visualize:

$$\log_{10} \mathrm{CCDF}(x; I).$$

Residual samples were aggregated across 4 Monte Carlo realizations per intensity level to stabilize empirical tail estimates.

Figure 8 (3D). Tail suppression surface: log-CCDF of residual norms vs intensity

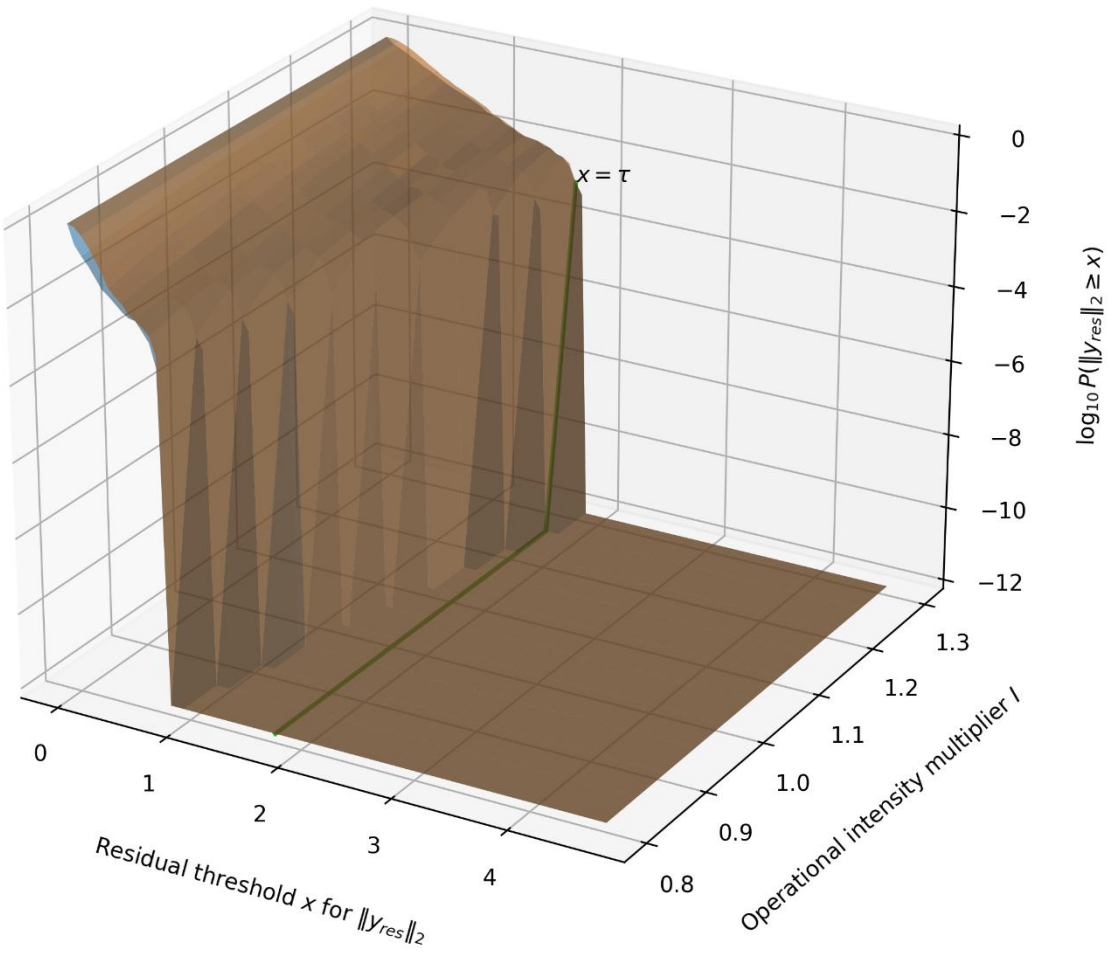


Figure 8 | Tail suppression surface

Figure 8 shows the surface:

$$(x, I) \mapsto \log_{10} P(\| y_{\text{res}} \|_2 \geq x).$$

Two structural effects emerge:

1. **Tail steepening:**
   The symmetry-aligned allocation produces faster decay of the CCDF in the high-threshold region.

2. **Intensity decoupling:**
   As intensity increases, the unaligned controller exhibits thickening of the residual tail, whereas the aligned controller maintains significantly reduced tail mass beyond the operational threshold $x = \tau$.

The vertical ridge at $x = \tau$ highlights the operational boundary used in CDI estimation, demonstrating that symmetry alignment reduces exceedance probability not only at a single threshold but across the entire high-amplitude regime.

Consider discrete excitation

$$y_k = \alpha y_{k-1} + \epsilon_k, \epsilon_k \sim \mathcal{N}(0, \sigma^2 I).$$

Stationary covariance:

$$\Sigma_y = \frac{\sigma^2}{1 - \alpha^2} I.$$

Closed-loop dynamics:

$$x_{k+1} = A_c x_k + G\epsilon_k.$$

Stationary covariance solves discrete Lyapunov equation:

$$\Sigma_x = A_c \Sigma_x A_c^\top + GG^\top.$$

Residual moment:

$$y_{\text{res}} = Cx, \Sigma_{\text{res}} = C\Sigma_x C^{\top}.$$

Proposition 4.1 (Sub-Gaussian Bound)

For any $\tau > 0$,

$$\mathbb{P}(\| y_{\text{res}} \|_2 \geq \tau) \leq \mathrm{e}^{\left(-\frac{\tau^2}{2\lambda_{\max}(\Sigma_{\text{res}})}\right)}.$$

tail decay rate is governed by the maximal eigenvalue of the residual covariance. Since the closed-loop system is linear and driven by Gaussian excitation, the stationary state is Gaussian, and residual moments are sub-Gaussian.

Let $\Sigma_{\text{res}}^{\text{unaligned}}$ and $\Sigma_{\text{res}}^{\text{aligned}}$ denote stationary covariances under the two allocation strategies.

Theorem 4.2 (Tail Suppression via Invariant Allocation)

If

$$\lambda_{\max}(\Sigma_{\text{res}}^{\text{aligned}}) < \lambda_{\max}(\Sigma_{\text{res}}^{\text{unaligned}}),$$

then for sufficiently large thresholds,

$$\mathbb{P}_{\text{aligned}}(\| y_{\text{res}} \|_2 \geq \tau) \leq \mathbb{P}_{\text{unaligned}}(\| y_{\text{res}} \|_2 \geq \tau).$$

Hence symmetry-aligned allocation yields uniformly sharper exponential tail decay.

This provides analytical justification for exceedance-surface curvature and CCDF steepening observed numerically.

Interpretation

Figures 7–8 collectively establish that symmetry-aligned allocation:

- Reduces operational exceedance probability,

- Suppresses high-amplitude residual tail events,
- Maintains robustness under actuator effectiveness uncertainty,
- Exhibits slower risk growth across turbulence intensity regimes.

This provides quantitative operational validation of the symmetry-induced stabilization principle in stochastic aerodynamic environments.

Control commands are obtained via constrained least-squares [2,5,13]:

$$u^* = -B_{\text{mom}}^{\dagger} y.$$

Rate limits and saturation are then applied. This strategy ignores symmetry-channel structure.

Moment components are compensated independently:

$$u^+ = -(B^+)^{\dagger} y^+, u^- = -(B^-)^{\dagger} y^-,$$
$$u = Su^+ + Au^-.$$

Constraints are applied identically to the unaligned case.

This enforces allocation within invariant subspaces defined by system symmetry.

Simulations are performed using forward Euler integration with timestep:

$$\Delta t = 0.02 \text{ s},$$

over a 30-second horizon.

Stochastic realizations use fixed random seeds for reproducibility.

Robustness analysis perturbs actuator effectiveness as

$$B_{\text{mom}} \to B_{\text{mom}}(1 + \delta), \delta \in [-\epsilon, \epsilon].$$

Peak residual moments are computed as

$$\max_t \| y(t) \|.$$

RMS metrics are computed over the full simulation horizon

5. Discussion

The results demonstrate that turbulence-induced destabilization in symmetric physical systems is governed not solely by disturbance magnitude, but by how disturbance projections couple into symmetry-defined load subspaces. In the present model, stochastic gust excitation generates broadband fluctuations in aerodynamic moments. However, destabilizing behavior is concentrated in low-dimensional parity channels corresponding to the system's geometric symmetry.

The primary mechanism underlying performance improvement is the structural separation of control allocation across these channels. In the unaligned strategy, constrained least-squares allocation operates directly in full moment space. Because actuator effectiveness exhibits inherent parity structure, this unconstrained projection induces cross-channel coupling. Under bounded authority and rate limits, such coupling leads to premature saturation in dominant antisymmetric modes and incomplete cancellation of residual loads.

By contrast, symmetry-channel aligned allocation enforces decomposition at the level of moment projections. Compensation is performed independently within symmetric and antisymmetric subspaces. This reduces projection loss, preserves effective control authority within each channel, and prevents destructive interference between parity modes. The result is a systematic reduction in both peak and RMS load magnitudes under identical actuation constraints.

Importantly, the improvement does not arise from increased control energy. Total integrated actuation effort increases marginally relative to the unaligned strategy, yet saturation time decreases significantly. This indicates that performance gains derive from geometric redistribution of control authority rather than aggressive actuation. The mechanism is therefore structural rather than energetic [6,10].

The robustness results further clarify the geometric origin of stabilization. Under bounded perturbations in actuator effectiveness, unaligned allocation exhibits pronounced degradation. This is consistent with sensitivity of pseudo-inverse solutions to column-space perturbations when projections are not parity-aligned. Symmetry-channel separation reduces this sensitivity by

constraining allocation within orthogonal subspaces. As predicted by the theoretical framework, the reduction in cross-coupling directly improves robustness margins.

These findings support the central claim of the Symmetry-Induced Stabilization Principle: in symmetric dynamical systems, destabilizing moments decompose along symmetry-defined channels, and stabilization efficiency increases when control redistribution respects that decomposition.

Interpretation in the Context of Turbulence

The present results do not imply suppression of turbulence in the fluid-dynamic sense. The gust field remains stochastic and broadband. Instead, the mechanism operates at the level of structural load projection. Turbulent energy continues to excite the system, but its destabilizing projection onto rigid-body and modal coordinates is reduced through channel-aligned redistribution.

This distinction is essential. The principle does not alter Navier–Stokes dynamics or eliminate turbulent structures [1,22]. Rather, it modifies how structural geometry and distributed actuation interact with those structures. Stabilization occurs in load space, not in flow space.

Consequently, the framework is compatible with classical turbulence theory. It does not contradict dissipation-based models; instead, it complements them by identifying a geometric pathway for reducing load amplification under bounded control authority.

Generality of the Principle

Although demonstrated in a minimal gust–aeroelastic model, the principle extends to any symmetric physical system in which:

1. Disturbance effects project into a finite-dimensional load or force space,
2. Actuation authority is distributed across symmetric elements,
3. Stabilization is achieved via constrained allocation rather than full-state cancellation.

Examples include symmetric flexible structures, rotorcraft blade systems, satellite appendages, and distributed propulsion configurations. In each case, destabilizing loads admit parity decomposition, and allocation aligned with that decomposition reduces cross-coupling inefficiencies.

The generality arises from group-theoretic structure rather than aerodynamic specifics. Any system admitting a discrete symmetry group Γ will exhibit invariant subspaces under its representations. Stabilization becomes a problem of allocation within these invariant subspaces.

Beyond mechanical systems, the underlying mathematics is not domain-specific. Any networked dynamical system admitting a discrete symmetry group Γ and distributed actuation or redistribution mechanisms will exhibit invariant subspaces under the action of Γ; fluctuations projecting into low-dimensional imbalance coordinates can, in principle, be systematically reduced through symmetry-aligned allocation within these invariant subspaces [16,21,28].

Limitations

Several limitations should be acknowledged.

First, the validation employs a reduced-order linear model. While sufficient to demonstrate the geometric mechanism, it does not capture nonlinear aerodynamic effects, flow separation, or high-angle-of-attack dynamics. Extension to nonlinear regimes requires further investigation.

Second, symmetry-channel separation assumes approximate geometric symmetry. Real airframes may exhibit asymmetries due to manufacturing tolerances, damage, or configuration changes. The robustness analysis indicates tolerance to moderate effectiveness perturbations, but severe symmetry breaking may degrade performance.

Third, the present allocation strategy relies on full measurement or estimation of load vectors. Implementation in practical systems would require reliable sensing and estimation under noise and latency constraints.

Finally, the analysis focuses on bounded actuator authority typical of conventional control surfaces. Systems with highly asymmetric actuator placement may not benefit equivalently from channel decomposition.

Conclusion of the Discussion

The central insight of this work is that stabilization in symmetric dynamical systems is fundamentally a geometric problem of projection and redistribution. When turbulence-induced loads are decomposed along symmetry-defined channels, control allocation that respects those channels improves efficiency, reduces saturation, and enhances robustness under uncertainty.

This mechanism operates independently of turbulence suppression and does not require increased control energy. It arises from alignment between system symmetry and actuation redistribution.

The results therefore establish symmetry as a structural pathway to dynamical resilience under stochastic excitation.

References

1. Batchelor, G. K. *The Theory of Homogeneous Turbulence* (Cambridge Univ. Press, 1953).
2. Ben-Israel, A. & Greville, T. N. E. *Generalized Inverses: Theory and Applications* (Springer, 2003).
3. Bisplinghoff, R. L., Ashley, H. & Halfman, R. L. *Aeroelasticity* (Addison–Wesley, 1955).
4. Bloch, A. M., Krishnaprasad, P. S., Marsden, J. E. & Murray, R. M. Nonholonomic mechanics and symmetry. *Arch. Ration. Mech. Anal.* **136**, 21–99 (1996).
5. Bodson, M. Evaluation of optimization methods for control allocation. *J. Guid. Control Dyn.* **25**, 703–711 (2002).
6. Bullo, F. & Lewis, A. D. *Geometric Control of Mechanical Systems* (Springer, 2004).
7. Dörfler, F., Chertkov, M. & Bullo, F. Synchronization in complex oscillator networks and smart grids. *Proc. Natl Acad. Sci. USA* **110**, 2005–2010 (2013).
8. Dowell, E. H. *et al. A Modern Course in Aeroelasticity* (Springer, 2014).
9. Durham, W. C., Bordignon, K. A. & Beck, R. *Aircraft Control Allocation* (Wiley, 2017).
10. Field, M. *Dynamics and Symmetry* (Imperial College Press, 2007).
11. Härkegård, O. Flight control design using backstepping and control allocation. *Linköping Stud. Sci. Technol.* (2003).
12. Hoblit, F. M. *Gust Loads on Aircraft: Concepts and Applications* (AIAA, 1988).
13. Johansen, T. A. & Fossen, T. I. Control allocation—a survey. *Automatica* **49**, 1087–1103 (2013).
14. Livne, E. Aircraft active flutter suppression: state of the art and technology maturation needs. *J. Aircr.* **55**, 410–452 (2018).
15. Marsden, J. E. & Ratiu, T. S. *Introduction to Mechanics and Symmetry* (Springer, 1999).
16. Mesbahi, M. & Egerstedt, M. *Graph Theoretic Methods in Multiagent Networks* (Princeton Univ. Press, 2010).
17. Mukhopadhyay, V. Historical perspective on analysis and control of aeroelastic responses. *J. Guid. Control Dyn.* **26**, 673–684 (2003).
18. Nishikawa, T. & Motter, A. E. Symmetric states requiring system asymmetry. *Phys. Rev. Lett.* **117**, 114101 (2016).
19. Olver, P. J. *Applications of Lie Groups to Differential Equations* (Springer, 1993).

20. Pecora, L. M. & Carroll, T. L. Master stability functions for synchronized coupled systems. *Phys. Rev. Lett.* **80**, 2109–2112 (1998).

21. Pecora, L. M., Sorrentino, F., Hagerstrom, A. M., Murphy, T. E. & Roy, R. Cluster synchronization and isolated desynchronization in complex networks with symmetries. *Nat. Commun.* 5, 4079 (2014).

22. Pope, S. B. *Turbulent Flows* (Cambridge Univ. Press, 2000).

23. Serrin, J. On the interior regularity of weak solutions of the Navier–Stokes equations. Arch. Ration. Mech. Anal. **9**, 187–195 (1962).

24. Stewart, I., Golubitsky, M. & Pivato, M. Symmetry groupoids and patterns of synchrony in coupled cell networks. *SIAM J. Appl. Dyn. Syst.* 2, 609–646 (2003).

25. Temam — *Navier–Stokes Equations: Theory and Numerical Analysis* (AMS Chelsea, 2001)

26. Trefethen, L. N. & Bau, D. *Numerical Linear Algebra* (SIAM, 1997).

27. Von Kármán, T. Progress in the statistical theory of turbulence. *Proc. Natl Acad. Sci. USA* **34**, 530–539 (1948).

28. Wright, J. R. & Cooper, J. E. *Introduction to Aircraft Aeroelasticity and Loads* (John Wiley & Sons, 2007).

29. Zaccarian, L. & Teel, A. R. *Modern Anti-windup Synthesis: Control Augmentation for Actuator Saturation* (Princeton Univ. Press, 2011).

30. Zelazo, D. & Mesbahi, M. Edge agreement: graph-theoretic performance bounds and passivity analysis. *IEEE Trans. Autom. Control* **56**, 544–555 (2011).